Sound & Vibration 2026, 60(5), 4590.
doi: https://doi.org/10.59400/sv4590

Article

Dynamic characterization and vibration response of high-speed milling for A2024-T351 aluminum alloy

Rami Smari, Ltaief Lammari*, Ali Rakrouk, Ali Arfaoui, Sana BenKhlifa

Laboratory of Mechanical and Agro-Industrial Engineering, Medjez El Bab Higher School of Engineering, University of Jendouba, Jendouba 8189, Tunisia

*** Corresponding author:** Ltaief Lammari, ltaief.laamari@esim.u-jendouba.tn

CITATION

Smari R, Lammari L, Rakrouk A, et al. Dynamic characterization and vibration response of high-speed milling for A2024-T351 aluminum alloy. Sound & Vibration. 2026; 6(5): 4590.
https://doi.org/10.59400/sv4590

ARTICLE INFO

Received: 30 June 2026
Revised: 23 July 2026
Accepted: 30 July 2026
Available online: 18 August 2026

Abstract: A coupled finite element–finite difference framework was developed to simulate high-speed peripheral milling of A2024-T351 aluminum alloy, enabling the analysis of chip formation, thermal gradients, and dynamic instability. The finite element model was used to predict the thermo-mechanical response and chip formation, while the finite difference formulation was employed to solve the transient heat transfer under different cutting conditions. The workpiece plastic deformation was described using a Johnson–Cook (JC) constitutive law coupled with a cumulative damage model, whereas the tungsten carbide (WC) cutting tool was modeled as a thermo-elastic body. Mesh and time-step sensitivity analyses were performed to ensure numerical convergence and solution stability. Thermal fields and structural responses were evaluated as functions of cutting speed, feed rate, depth of cut, and milling strategy (climb and conventional). Time-resolved cutting force signals were analyzed using the fast Fourier transform (FFT) to correlate local chip segmentation with macroscopic vibration modes. The results showed that the maximum temperature stabilized after the engagement of the fourth tooth (739.6–742.5 K), with the majority of generated heat dissipated through chip evacuation. Compared with conventional milling, climb milling reduced the peak contact temperature by 6.5% and resulted in a smoother harmonic force response. Spectral analysis further showed a clear separation between the tooth-passing frequency (600 Hz) and the thermomechanical chip segmentation frequency (1,850 Hz). The numerical predictions were validated against experimental cutting parameter measurements, showing deviations below 5%. The proposed framework provides an effective predictive tool for analyzing high-speed milling and identifying cutting conditions that reduce structural vibration while maintaining thermal and mechanical performance.

Keywords: numerical simulation; milling process; high-speed machining (HSM); heat generation; surface finish; structural dynamics; vibration control; frequency analysis

1. Introduction

The HSM is considered one of the most important fundamental technologies in modern manufacturing due to the advantages it offers in terms of productivity, dimensional accuracy and surface integrity compared to conventional machining [1]. When machining at cutting speeds far above those used in conventional machining, high material removal rates can be achieved with concurrent reductions in cutting forces, chip thickness, and overall machining time [1]. These advantages make the HSM particularly suitable for aerospace and automotive industries [2] where lightweight alloys and precision components are predominantly employed. For such materials, high specific strength and outstanding fatigue resistance make aluminum alloy A2024-T351 widely machined and used for structural components [3].

However, in peripheral milling, the finishing operation leads to non-linear physical complexities. Intense plastic deformation of the surface and frictional sliding motion produce heat generation that is strongly localized in a small volume. While most of this thermal energy is carried away by the chips, although the majority of the heat is dissipated by the chips, the intermittent nature of milling makes temperature control more challenging. For this reason, numerical simulations are usually adopted to analyse temperature distribution and to predict chip behaviour during high-speed milling [4]. Since the seminal work of Kalamecki [5], who applied the Lagrangian finite element technique to model machining, numerous models have been developed to study chip formation, plastic flow in the workpiece and tool wear [6]. In addition, authors investigated the separate contribution of tool geometries using HSM [7] and interfacial friction [8]. However, an exact analytical treatment of the frictional problem at the tool-workpiece-chip interface is difficult due to the uncertainties in evaluating the heat flux-sensitive parameters, the thermal contact conductance, and the fraction of heat partition among the contact bodies.

In addition to the thermo-mechanical phenomena, the discontinuous chip formation occurring during HSM of A2024-T351 generates cyclic variations of the cutting force, which may excite the dynamic response of the machine-tool system and, under adverse circumstances, leads to machining instabilities such as chatter and surface waviness [9]. Consequently, characterizing the frequency content of these cutting force fluctuations is essential for assessing the dynamic stability of the machining process and identifying the underlying vibration mechanisms [10].

Therefore, the present study aims to develop a comprehensive numerical framework to investigate the coupled thermo-mechanical and dynamic behavior of high-speed peripheral milling of A2024-T351 aluminum alloy using a tungsten carbide cutting tool. The effects of cutting parameters, including cutting speed, feed rate, and depth of cut, as well as milling configuration (climb and conventional milling), are systematically investigated. In addition, FFT analysis of time-resolved cutting forces is performed to identify the relationship between tooth engagement effects, chip segmentation phenomena, and dynamic excitation frequencies. The proposed numerical approach is validated through comparison with experimental measurements, demonstrating its capability to accurately capture the main thermo-mechanical and dynamic characteristics of the high-speed milling process.

The remainder of this paper is organized as follows. Section 2 presents the numerical methodology, including the material constitutive model, damage formulation, contact conditions, thermal analysis, and experimental validation procedure. Section 3 discusses the obtained results, focusing on chip formation mechanisms, temperature evolution, and cutting-force behavior under various machining conditions. In addition, FFT-based frequency analysis is conducted to investigate the dynamic characteristics of the cutting forces and to identify the relationship between tooth engagement effects, chip segmentation phenomena, and vibration response. Finally, Section 4 summarizes the main findings of the study and provides conclusions regarding the thermo-mechanical and dynamic behavior of high-speed milling of A2024-T351 aluminum alloy.

2. Materials and methods

2.1. Numerical modeling of the high-speed machining process

Simulating HSM processes, such as peripheral milling, requires an advanced numerical scheme capable of handling severe plastic deformation and rapid thermal gradients. In this study, a non-linear finite element model was developed utilizing an explicit dynamic time integration scheme coupled with a temperature-displacement formulation.

A Lagrangian description was adopted to accurately track the material deformation, tool-workpiece interaction, and geometric chip formation [11]. To optimize computational efficiency while capturing the essential multi-physical phenomena, a 2-D plane strain formulation was selected. This approach effectively accounts for the thermal effects generated within the primary and secondary shear zones, which significantly modulate the mechanical behavior of the material [12].

The material behavior of the workpiece was modeled using the constitutive and damage formulations of JC [13] to evaluate their impact on thermal evolution and surface integrity. Given the explicit nature of the dynamic solver, the predicted cutting force history is inherently a time-resolved dynamic signal, capturing high-frequency fluctuations induced by chip segmentation and intermittent tooth engagement.

To analyze the dynamic and vibratory content of the process, the simulated cutting force time-history $F(t)$ was post-processed using a Discrete FFT to transition from the time domain to the frequency domain [14]:

$$P(f) = \left| \int_{-\infty}^{+\infty} F(t) \, e^{-i2ft} dt \right| \tag{1}$$

This spectral analysis enables the identification of dominant excitation frequencies associated with chip segmentation mechanisms. These frequencies were systematically compared to the characteristic tooth-passing frequency (f_x), computed from the spindle speed (N in rpm) and the number of teeth (z) as follows [15]:

$$f_x = \frac{N \cdot z}{60} \tag{2}$$

This comparison serves to evaluate the susceptibility of the machine-tool system to forced vibrations and regenerative chatter.

2.2. Constitutive equations and material properties

2.2.1. Workpiece material (A2024-T351)

The material selected for the workpiece is A2024-T351. The choice of such material is justified by the advantages it offers in terms of thermal softening strength and viscoplastic behaviour, both of which are essential to accurately capturing chip formation during the cutting [3]. The mechanical and temperature- dependent thermal properties are listed in **Table 1** [16].

Table 1. Mechanical and thermal properties of A2024-T351.

Material properties	Values	Units
Density	2,700	Kg·m^{-3}
Elastic Modulus	73	GPa
Poisson's Ratio	0.33	-
Specific Heat	0.55 T + 877.6	J/kg/°C
Thermal Conductivity	For 25 ≤ T ≤ 300: 0.247 T + 114.4 For 300 ≤ T ≤ 520: 0.125 T + 226.0	W/m.°C
Expansion	8.9 × 10^{-3} T + 22.2	(μm.m/°C)
Melting Temperature	520	(°C)

To accurately reproduce the plastic flow and progressive failure of A2024-T351 under extreme strains, high strain rates, and elevated temperatures, the Johnson–Cook constitutive plasticity model was implemented [17]. The model considers the effects of strain hardening, strain-rate dependency, and thermal softening, and is given by the following equivalent flow stress σ [18]:

$$\sigma = (A + B\varepsilon^n)\left(1 + C\ln\frac{\dot{\varepsilon}}{\dot{\varepsilon_0}}\right)[1 - \left(\frac{T - T_r}{T_m - T_r}\right)^m] \quad (3)$$

Where ε is the equivalent plastic strain, $\dot{\varepsilon}$ is the plastic strain rate, $\dot{\varepsilon}_0$ is the reference strain rate, T is the current temperature, T_{room} is the ambient temperature, and T_{melt} is the melting temperature. The constants A, B, n, C, and m represent the yield stress, hardening modulus, strain hardening exponent, strain rate sensitivity coefficient, and thermal softening exponent, respectively.

Furthermore, chip separation and material failure were governed by the JC cumulative damage law. This law is based on the assumption that the equivalent plastic strain at fracture is influenced by the stress triaxiality, strain-rate effects, and temperature. The strain at failure ε_f is defined by Gunsalam et al. [18]:

$$\varepsilon_f = \left[D_1 + D_2\exp\left(D_3\frac{\sigma_m}{\sigma}\right)\right]\left[1 + D_4\ln\left(\frac{\dot{\varepsilon}}{\dot{\varepsilon}_0}\right)\right]\left[1 + D_5\left(\frac{T - T_{\text{room}}}{T_{\text{melt}} - T_{\text{room}}}\right)\right] \quad (4)$$

Where $\frac{\sigma_m}{\sigma}$ is the stress triaxiality ratio, and D_1–D_5 are the material failure parameters.

The parameters of the JC constitutive and damage models, given by Equations (3) and (4), respectively, were selected from the literature [16], as summarized in **Table 2**.

Table 2. Johnson-Cook parameters for A2024-T351.

Johnson-Cook plasticity parameters				
A (MPa)	B (MPa)	n	C	m
352	440	0.42	0.0083	1
Johnson-Cook damage parameters				
D1	D2	D3	D4	D5
0.13	0.13	−1.5	0.011	0

2.2.2. Cutting tool material

The cutting tool is modeled as a Tungsten Carbide insert. This material was selected due to its exceptionally high stiffness, hardness, and negligible plastic deformation under severe machining conditions [19]. Because it does not exhibit significant strain hardening or thermal softening within the operational envelope of this study [20], the Johnson–Cook viscoplastic law was omitted for the tool. Consequently, the tool was treated using a purely thermo-elastic formulation. The thermal and mechanical properties governing the cutting tool behavior are provided in **Table 3** [21].

Table 3. Mechanical and thermal properties of the tungsten carbide.

Material properties	Value	Units
Density	11,900	kg/m^3
Elastic Modulus	534	GPa
Poisson's Ratio	0.22	-
Specific Heat	400	J/kg/°C
Thermal Conductivity	50	W/m/°C

2.3. Simulation setup

In the present simulation, the workpiece was modeled as a large rectangular block fixed at its base to prevent all movement and meshed using CPE4RT elements, which are four node, plane-strain, thermally coupled elements with reduced integration (see **Figure 1**).

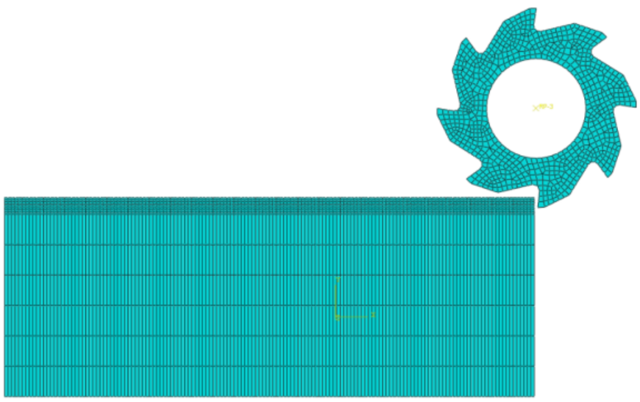

Figure 1. Model mesh.

The selection of the CPE4RT element formulation is due to its capability to simultaneously solve the mechanical deformation and heat transfer fields during the cutting process [22]. The coupled formulation provides stable prediction of the high temperature gradients generated at the tool–chip interface [23], where intense plastic deformation and frictional heat generation occure, while maintaining numerical stability under the transient conditions encountered in HSM.

The workpiece was subdivided into three sections: the chip formation zone, the separation zone and the remaining bulk material (see **Figure 2**). The first section (1) represents the layer of the material that was removed during the milling, and it defines the cutting depth. The second section (2) consists of a very thin layer which facilitates chip removal. The third section (3) corresponds to the unimpacted layer of the workpiece.

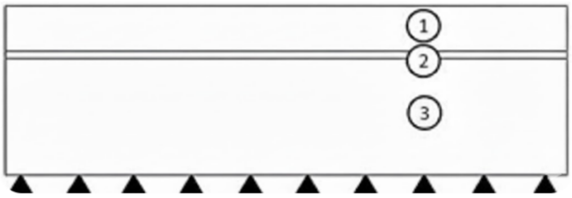

Figure 2. Workpiece geometry and boundary conditions.

A refined mesh was applied in both chip formation and separation zones due to the strong localization of deformation, temperature gradients, and damage evolution in these areas [24]. Although adaptive remeshing can reduce computational requirements, it was not considered in the present study due to the risk of losing the continuity of history-dependent variables during mesh reconstruction, such as plastic strain, temperature, and JC damage. Therefore, a localized mesh refinement strategy was adopted to achieve reliable chip formation prediction while reducing the computational cost.

With the aim of allowing the heat transfer of the cutting tool and its impact on the workpiece, it was developed as a 2D deformable body. It was meshed using both CPE4RT elements and CPE3T elements, which are 3-node plane strain thermally coupled triangle elements. These thermally coupled elements allow simultaneous resolution of mechanical deformation and temperature evolution during machining [25]. The mesh was also refined in the cutting edges of the milling tool (see **Figure 1**).

The cutting tool movement was governed by a rigid body constraint applied on the reference point, preventing elastic deformation. Two boundary conditions have been assigned to the reference point: a translation velocity V_c defining the feed direction and angular velocity ω enforcing the desired cutting speed (see **Figure 3**). Thus, the tool's movement was defined by the imposed cutting speed and feed rate along with the depth of cut. Parametric studies were conducted on these key variables to analyze their influence on temperature, cutting forces, and chip formation (**Table 4**).

Figure 3. Tool geometry and boundary conditions.

Table 4. Cutting parameters.

Parameter	Value 1	Value 2	Value 3
Cutting Speed (m/s)	10	15	20
Cutting Depth (mm)	0.5	1.5	2
Feed Rate (mm/min)	500	1,000	2,000

A contact surface has been defined between the tool and the workpiece where both friction and thermal interaction are applied to capture heat generation, stress distribution, and chip formation during cutting.

2.4. Experimental study

In order to validate the numerical prediction, an experimental plan was conducted on an OPTImill MT50 milling machine (see **Figure 4**). A2024-T351 workpieces were machined using a tungsten carbide cutting tool that has the same geometry as the one used in the numerical model. Similar to the simulation, the cutting speed was varied to evaluate the influence of strain rate and thermal effects. High-speed optical imaging was used to document chip formation and shear zone development, and a Fluke Ti27 infrared camera was used to measure the temperature and capture its distribution (see **Figure 4**).

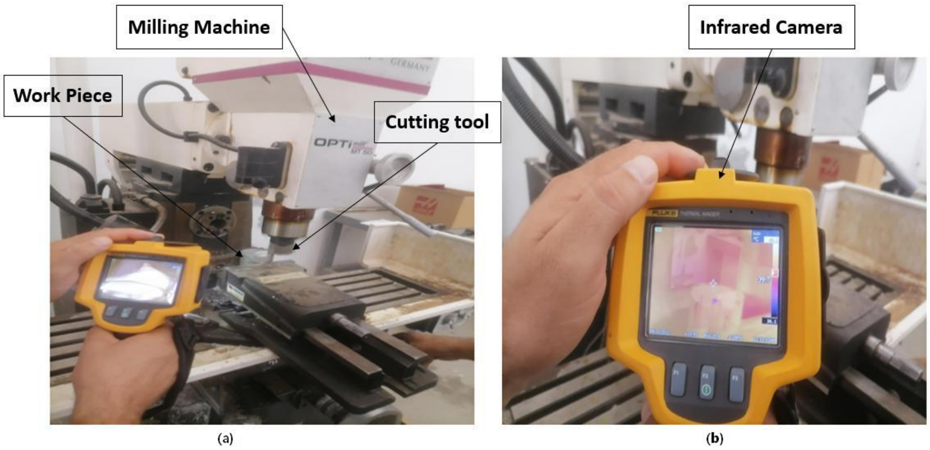

Figure 4. Experimental setup: **(a)** OPTImill MT50 milling machine; **(b)** Fluke Ti27 infrared camera.

The obtained experimental results were compared with the numerical ones, allowing a comprehensive evaluation of the model's robustness.

3. Results and discussion

This simulation is essentially based on two main aspects: analysis of chip formation and the influence of the cutting parameters and their variation on the model.

Chip formation is first examined to characterize the material deformation and chip morphology obtained under the considered conditions.

Although several parameters may affect the cutting temperature and intervene directly or indirectly in its evolution, the present study is limited to the most significant cutting parameters while the remaining parameters are maintained constant. Therefore, the analysis focuses on cutting speed, feed rate and depth of pass along with the mode of action of the milling cutter (milling by swallowing or milling in opposition).

The following sections provide a comprehensive analysis of the simulation outcomes and the results of these aspects.

3.1. Analysis of chip formation

The HSM of the A2024-T351 revealed that the chip formation occurs in a discontinuous manner (see **Figure 5**). After the cracking of the material at the beginning of the cutting, the simulation captured the formation and the evacuation of the chip. **Figure 5** shows the temperature distribution during the first pass. This distribution revealed that the majority of generated heat is carried away by the chip, while the remaining heat is transferred to both the tool and the workpiece, with the temperature slightly higher in the contact zone between the workpiece and the cutting edge, reaching approximately 487.6 °C at the end of the pass, and close to the ambient temperature in the remaining surfaces. As a result, the thermal gradient became very steep, and the high temperature region was limited to specific areas.

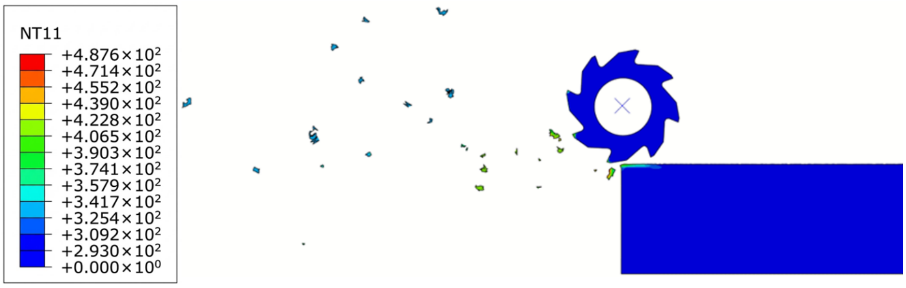

Figure 5. Heat distribution and chip formation during the first pass.

The observed fracture behavior can be attributed to the stress triaxiality effect incorporated in the JC damage model, which is influenced by the parameter D3 on the fracture strain. The negative value of this parameter (D3 = −1.5) used in this study indicates that the fracture strain decreases with increasing stress triaxiality. This behavior reflects the ductile fracture mechanism, where tensile hydrostatic stresses promote the initiation and growth of microvoids, leading to earlier material degradation and failure. During the machining process, the reduced fracture strain under tensile-dominated loading conditions enhances damage accumulation and facilitates chip separation when the damage variable reaches its critical value ($D = 1$). Consequently, the JC damage parameter D3 indirectly controls the energy release associated with chip fracture by controlling the initiation of material failure and element deletion during the numerical simulation.

3.2. Analysis of temperature evaluation

3.2.1. Effect of the cutting speed on the cutting temperature

The simulation results of the heat generated during the first contact between the tool and the workpiece showed a rise in the cutting temperature when the cutting speed was very high (see **Figure 6**). In fact, when varying the cutting speed from 10 m/s to 15 m/s, the temperature increased by about 2.73%. Meanwhile, when varying the cutting speed from 15 m/s to 20 m/s, the temperature rose from 496 K to 513.4 K; it can be seen that the temperature in the cutting zone has also increased significantly.

These results confirm that the increase in cutting speed causes an increase in friction and deformation, which raises the temperature in the cutting zone. The majority of the heat released from the cutting process is evacuated by the chip, and the heat exchanges with the part are minimal.

Figure 7 presents the formation of the first chip as the cutting tool engages the workpiece at different cutting speeds: 10 m/s, 15 m/s and 20 m/s. At a lower speed of 10 m/s, the chip is thicker compared to both other speeds. This is due to the fact that the material remains in contact with the cutting tool for a longer duration, providing sufficient time to deform plastically before separation. As the cutting speed increases, the chip becomes thinner and more continuous because of the increasing strain rates and the reduction of the contact time between the parts. It can also be seen that most of the heat generated is dissipated in the chips.

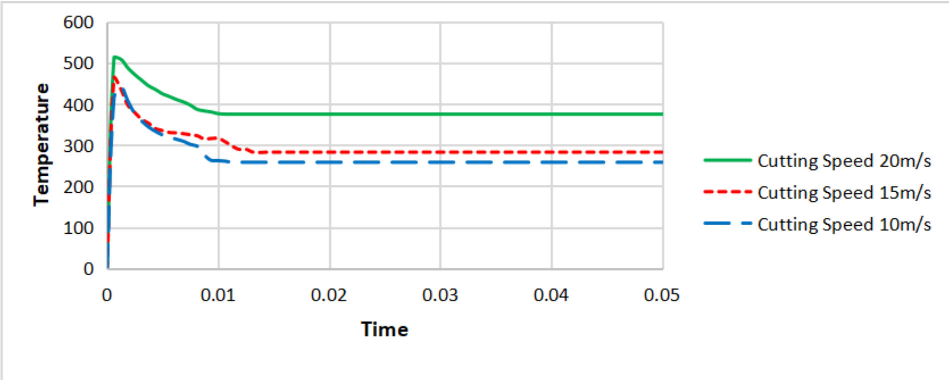

Figure 6. Evolution of the cutting temperature as a function of time.

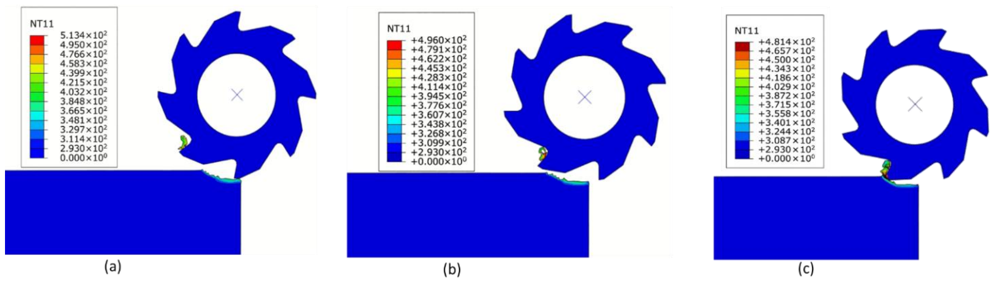

Figure 7. Chip formation and heat generation for: **(a)** cutting speed 20 m/s; **(b)** cutting speed 15 m/s; **(c)** cutting speed 10 m/s.

From the JC constitutive model's perspective, this chip morphology transition results from the combined effects of strain-rate sensitivity and thermal softening. The low value of the JC strain-rate sensitivity coefficient (C = 0.0083) limits the increase in flow stress associated with higher deformation rates, while the thermal softening exponent (m = 1.0) induces a significant reduction in material strength as the temperature rises. At higher cutting speeds, the heat generated by intense plastic deformation accumulates in the shear zone, which compensates for strain-rate hardening and facilitates material flow. Consequently, despite the high strain-rate conditions associated with high-speed machining, the thermal softening effect dominates, preventing severe adiabatic shear localization and promoting the formation of thinner and more continuous chips.

3.2.2. Effect of the feed rate on the cutting temperature

The results of increasing the feed rate from V_f = 500 mm/min to V_f = 1,000 mm/min and V_f = 2,000 mm/min, show an increase in temperatures (see **Figure 8**).

At 500 mm/min, the temperature is the lowest, reaching approximately 429 K. As the feed increases to 1,000 mm/min, the temperature rises noticeably to 436.45 K, with thicker chip formation and higher deformation energy. When the feed rate reaches 2,000 mm/min, the temperature reaches the highest value, which is 487.2 K.

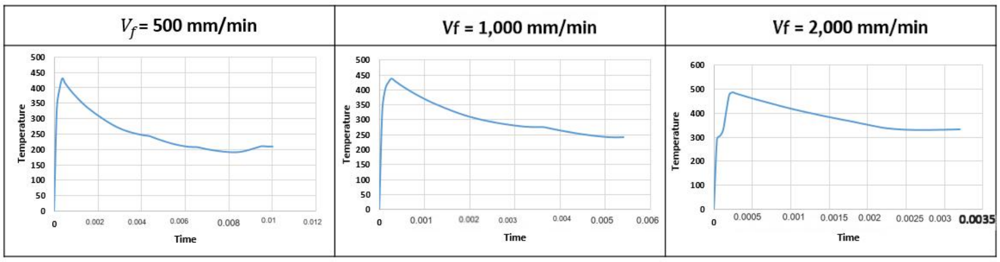

Figure 8. Effect of increasing the feed rate on the temperature.

This result can be justified by the increase in the cutting force and the chip thickness, which makes the material more resistant to rupture and requires greater effort for the removal of the chip and a high heat release.

3.2.3. Effect of the depth of cut on the cutting temperature

With the advantage of HSM, it becomes possible to increase the cutting depth compared to conventional machining; however, it also leads to an increase in the applied force, which generates an additional amount of heat.

Upon increasing the cutting depth of our model, it was noted that the cutting temperature was significantly influenced (see **Figure 9**). As the depth of cut increases from 0.5 mm to 1.5 mm, the temperature also increases by 6%. And the increase in depth from 1.5 mm to 2 mm resulted in a temperature rise of 3%. This heat elevation is justified by the fact that the volume of the removed material becomes larger, which leads to higher plastic deformation and higher friction between the tool and the workpiece, and as a result, the elevation of the cutting temperature and the increase in chip formation.

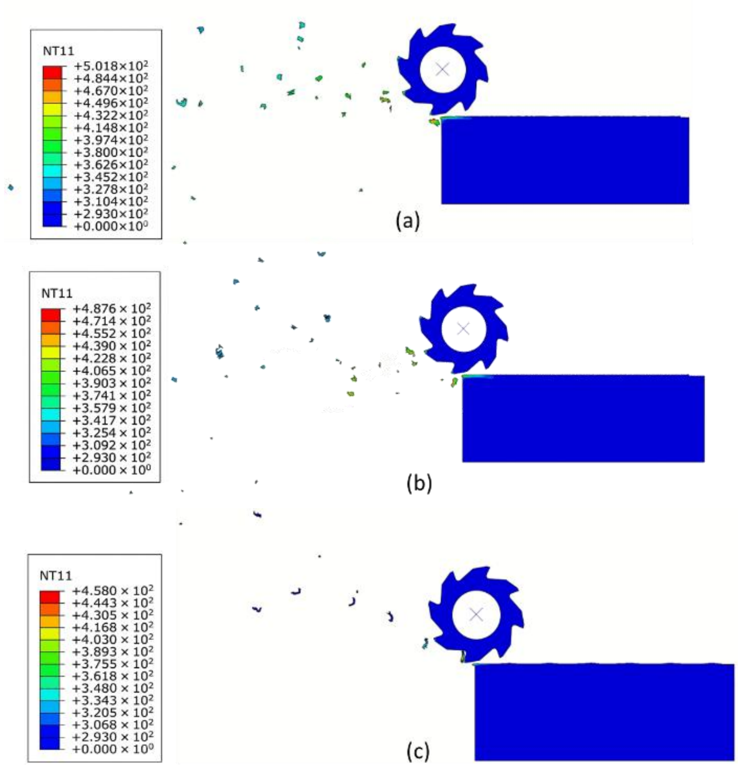

Figure 9. Chip formation and heat generation for: **(a)** cutting depth 2 mm; **(b)** cutting depth 1.5 mm; **(c)** cutting depth 0.5 mm.

3.2.4. Effect of the cutter action on thermal behavior

The orientation of the cutter, whether in opposition (conventional milling) or by swiping (climb milling), has a huge effect on the temperature:

The simulation of conventional milling, where the direction of feed is opposite to the direction of rotation of the tool (see **Figure 10**), highlighted the increase in temperature. This elevation is due to the hardening of the material as the tool begins to engage it. Instead of being cleanly sheared, the material became compressed and pushed before the chip could be formed. This intensifies friction between the tool and the workpiece, which leads to higher heat generation, poor surface condition and premature wear of the cutting tools.

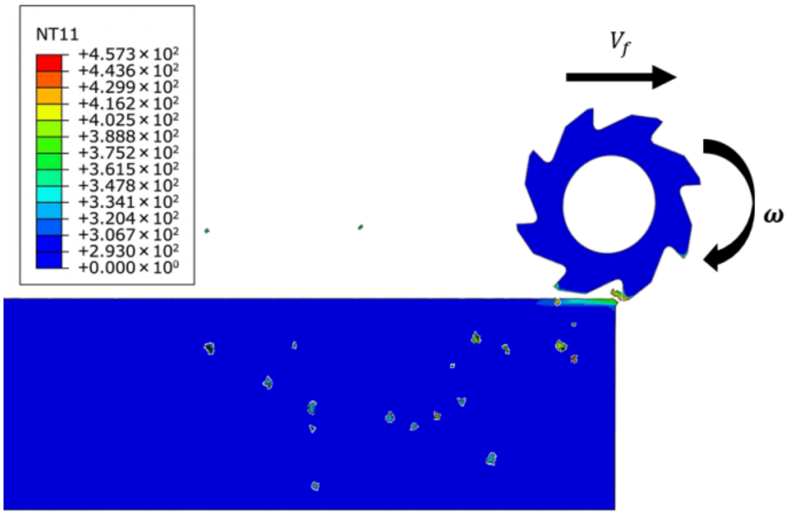

Figure 10. Milling in opposition.

Climb milling is when the feed direction is the same as the direction of rotation of the tool (see **Figure 11**). The simulation results show that the cutting temperature is lower than in opposition milling. This can be explained by the fact that the tool engaged with a higher chip thickness and reduced friction at the contact. Therefore, the chip was removed more efficiently, and the material was sheared instead of compressed. As a result, there was better surface condition and less heat generation.

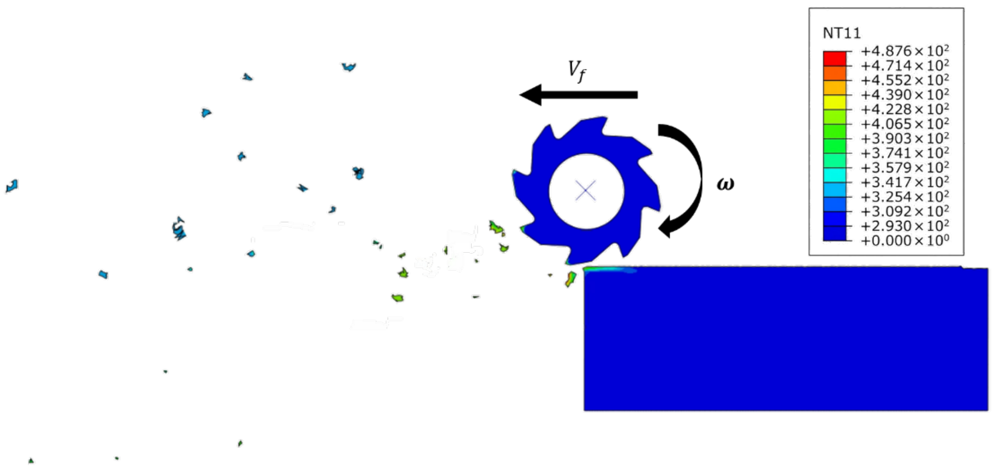

Figure 11. Milling by swallowing.

The comparison between the two milling orientations showed that milling by swallowing consistently resulted in a lower temperature, with a value of 457.3 K at the first tooth engagement, approximately 6.5% compared to the opposition milling, which has a temperature at first tooth engagement equal to 487.6 K.

3.2.5. Influence of the tool teeth engagement on the cutting temperature

The numerical results showed that, during the milling process, the generated temperature varies significantly from one tooth engagement to the other. **Table 5** presents the distribution of the temperature and the chip formation during the first contact of the workpiece and each tooth of the tool.

Table 5. Thermal distribution and chip formation at each tooth engagement.

Teeth	Temperature evaluation
1	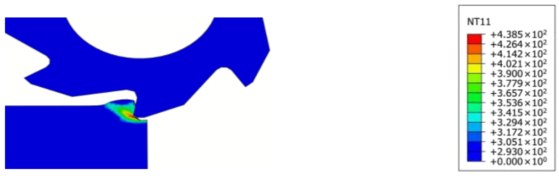
2	
3	
4	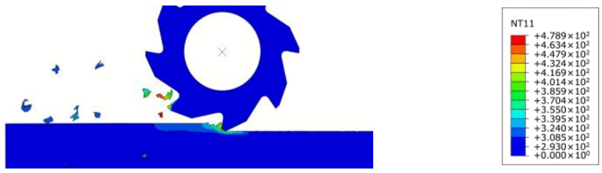
5	
6	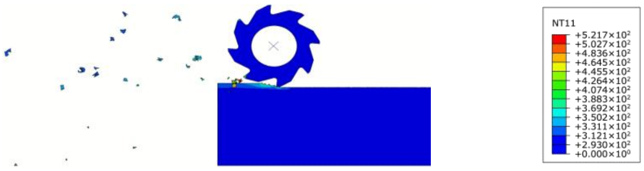
7	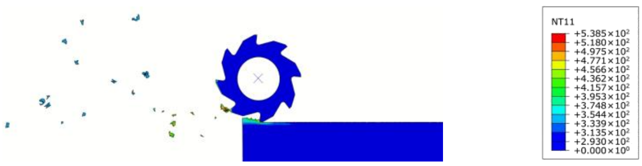

For the first tooth, the maximum temperature reached approximately 438.5 K. This peak value is lower compared to all the other teeth because the cutting tool engaged undeformed and colder material which limited the heat generation. When the second tooth reached the contact surface of the workpiece, the temperature slightly increased to around 446.5 K. This can be justified by the fact that the material has been partially heated and sheared, which led to an elevation in the maximum temperature. The temperature continues to increase until it reaches the end of the milling with a maximum value at first contact with the last tooth equal to approximately 538.5 K. At this stage, the cutting zone has accumulated heat from previous teeth with a stabilized chip formation.

Figure 12 shows the evolution of the maximum temperature reached at each tooth engagement in milling. During the first tooth engagement, the tool and the workpiece are cold, which explains, the low temperature. As the following teeth progressively engage with the workpiece, the temperature increases due to the repeated generation of heat from plastic deformation and tool–chip friction; the chip flow becomes more stable, and the shear zone becomes more thermally saturated. Therefore, each new tooth reaches a higher maximum temperature.

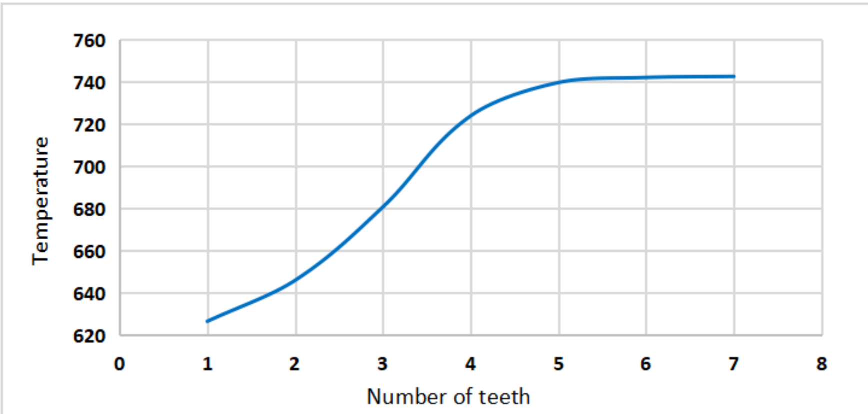

Figure 12. Evolution of the maximum temperature at each tooth engagement.

After approximately the fourth tooth engagement, the tool-workpiece interface reaches a thermal steady state varying within a narrow range of 739.6 K and 742.5 K. This stabilization indicates the achievement of a thermal balance between the heat generated during the cutting and the heat dissipation mechanisms. The heat produced in the shear zone is distributed among the cutting tool through conduction, the chip through heat transport during evacuation, and the workpiece through residual heat accumulation from successive tooth engagements. Once these mechanisms reach equilibrium, the remaining tooth engagements no longer result in significant temperature increases. The resulting steady-state temperature promotes thermal softening of the A2024-T351 alloy, reducing its flow stress and facilitating plastic deformation during subsequent cutting cycles.

3.3. Frequency response and dynamic analysis of cutting forces

3.3.1. Frequency analysis and vibration response

The discontinuous chip formation described in Section 3.1, together with the cyclic engagement and disengagement of the cutting edge during peripheral milling, generates a cutting force history that is inherently non-stationary and rich in harmonic content. To characterize this dynamic content, the simulated cutting force time history extracted from the ABAQUS/Explicit model was processed through an FFT, converting the time-domain signal into the frequency domain and revealing the dominant frequencies associated with chip breakage and successive tooth engagement.

For the reference configuration (15 m/s cutting speed, 1,000 mm/min feed rate, 1.5 mm depth of cut), the spectral analysis of the force signal showed a dominant low-frequency component corresponding to the tooth-passing frequency, consistent with the periodic engagement of successive teeth, together with higher-frequency harmonics attributable to the discontinuous, segmented nature of chip formation. The amplitude of these harmonics increased with cutting speed and feed rate, mirroring the trends already identified for temperature and chip thickness in Sections 3.2 and 3.3: configurations that produced thinner, more fragmented chips were also associated with a richer high-frequency content in the force spectrum, suggesting a stronger excitation of the higher structural modes of the tool-workpiece system.

Comparing the cutter action modes introduced in Section 3.3.2, the force signal obtained under climb milling (milling by swallowing) displayed a smoother, more periodic pattern with lower-amplitude harmonics than the signal obtained under conventional milling (milling in opposition), in agreement with the more efficient shearing and reduced friction already noted for climb milling. This indicates that, besides improving thermal performance and surface condition, climb milling is also expected to be more favourable from a dynamic stability standpoint, since it generates a less harmonically rich excitation of the machine-tool system.

From an acoustic standpoint, since airborne noise in high-speed machining is closely correlated with cutting force fluctuations, the spectral characteristics extracted from the force signal can be used as a first-order indicator of the acoustic emission expected during the process: configurations associated with higher-frequency, higher-amplitude harmonics in the force spectrum are expected to radiate more high-frequency acoustic energy, whereas the smoother force signal obtained under climb milling, at lower feed rate and cutting speed, is expected to be associated with reduced acoustic emission. While a direct acoustic measurement was beyond the scope of the present experimental setup, this frequency-domain correlation provides a basis for discussing the acoustic behaviour of the process from the available simulation data, and for guiding future experimental campaigns combining microphone or accelerometer measurements with the present numerical framework.

3.3.2. Dynamic and vibratory analysis of cutting forces

The dynamic behavior of the cutting force was investigated through the time evolution of the calculated cutting force component $Fx(t)$ over a representative time window of 30 ms. As shown in **Figure 13**, the cutting force exhibits periodic macro-oscillations varying between 220 N and 680 N. This periodic pattern results directly from the kinematics of the peripheral milling operation and, in particular, the regular and repetitive positioning of the three cutter teeth ($z = 3$) along the tool circumference. Since the cutting process involves the successive interaction of multiple teeth with the workpiece, the periodic variation of the engaged cutting edge results in a regular modulation of the cutting force. Furthermore, the non-zero minimum force observed during each cycle indicates that the cutting is continuous and the tool-workpiece engagement path is overlapped.

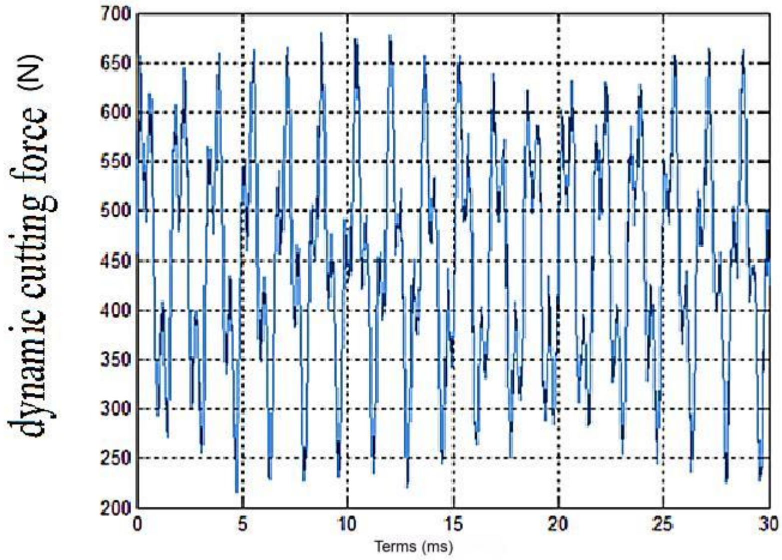

Figure 13. Simulated dynamic cutting force evolution showing periodic tooth engagement and high-frequency fluctuations.

In addition to this low-frequency periodic component, strong high-frequency fluctuations and sudden spikes of force take place. These abrupt force alterations are the micro-mechanical "footprints" of mainstream and secondary shear localized plastic instability (LPI) phenomenon. This cyclical behavior with its strongly competing effects of strain hardening and adiabatic thermal softening as described by the adopted JC constitutive relation (Equation (3)), which controls the transition from homogeneous plastic flow to serrated or segmented chip formation.

During high-speed machining, the strain-rate strengthening effect is activated by the increase in deformation rate, increasing the material flow stress through Equation (5)

$$\left(1 + C\ln\frac{\dot{\varepsilon}}{\dot{\varepsilon_0}}\right) \tag{5}$$

Conversely, the heat generated by severe plastic deformation under near-adiabatic conditions promotes thermal softening through the temperature-dependent Equation (6), reducing the material resistance to deformation.

$$1 - \left(\frac{T - T_r}{T_m - T_r}\right)^m \tag{6}$$

The interaction between these two mechanisms governs the stability of shear deformation and the initiation of adiabatic shear bands. For A2024-T351, the relatively low strain-rate sensitivity coefficient (C = 0.0083) limits the hardening contribution, while the thermal-softening exponent (m = 1.0) enhances the reduction of flow stress at elevated temperatures.

Consequently, thermal softening becomes dominant under the investigated cutting conditions, promoting periodic shear localization events that are reflected in the high-frequency force oscillations and influence the initiation frequency of serrated chip formation.

In order to separate and identify physical mechanisms responsible for the triggering of these tool dynamic forces (TDFs), a Discrete FFT was computed to obtain the power spectrum shown in **Figure 14**. Two dominant frequency components were identified, reflecting the different sources of dynamic excitation during machining. The first large peak appears at exactly 600 Hz (Equation (7)), which is the theoretical tooth-passing frequency calculated by Equation (2), where "N" is the spindle speed (rpm) and "z" is the number of cutter teeth. This frequency represents possible forced structural excitation at one gear tooth due to intermittent tooth-entry impacts.

$$f_x = \frac{N \cdot z}{60} = \frac{12{,}000 \times 3}{60} = 600 \text{ Hz} \tag{7}$$

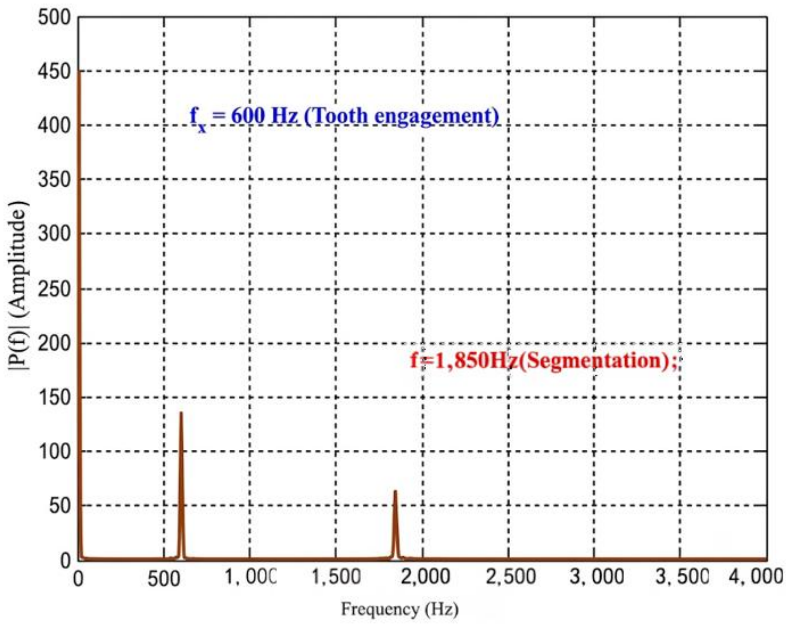

Figure 14. Discrete fast Fourier transform analysis identifying tooth-passing (f_x) and chip segmentation (f_c) frequencies.

The second dominant peak is observed around 1,850 Hz. Since this frequency is not a simple integer harmonic of the kinematic tooth-passing frequency, it is associated with the intrinsic chip segmentation frequency (f_c). The high-frequency peak emerges from the cyclic material fracture and release of strain energy governed by the fatigue damage rule.

The spectral separation between the chip segmentation frequency (f_c = 1,850 Hz), and the tooth-passing frequency (f_x = 600 Hz) demonstrates that the investigated cutting conditions do not promote strong dynamic coupling between tool engagement excitation and material-driven oscillations Consequently, the milling operation remains away from severe regenerative chatter conditions. However, when the chip segmentation frequency approaches an integer multiple of the tooth-passing frequency ($f_c \cong 3f_x$), the coupling between these two dynamic excitations can become amplified. Such synchronization may promote regenerative effects, where vibrations from one tooth pass modify the subsequent chip thickness, leading to increased force fluctuations and vibration amplitude. Therefore, the frequency relationship between tooth engagement and chip segmentation provides valuable insight into the dynamic stability of the milling process and the potential occurrence of chatter phenomena.

3.4. Comparison between numerical and experimental results

The numerical predictions from the finite element model were compared with experimental measurements to validate the model. **Table 6** summarizes the results for varying cutting speeds, feed rates, and the cutting depth. The small deviations, below 5%, of the results confirm the reliability of the model: the numerical model predicts a maximum temperature of 481.4 K and 496 K for simultaneously 10 m/s and 15 m/s cutting speeds, while the recorded temperatures are 497.25 K and 509.81 K. Similarly, the feed rate results have a deviation of approximately 3% and 4.5% for the respective feed rates 500 mm/min and 1,000 mm/min. The difference between the numerical and thermal results of the cutting depth has a variation below 2% for all the depths. With these results, the finite element model can be validated.

Table 6. Comparison between numerical and experimental results.

Cutting parameters		Numerical results (K)	Experimental results (K)
Cutting speed	10 m/s	481.4	497.25
	15 m/s	496	509.81
Feed Rate	500 mm/min	429	441.2
	1,000 mm/min	436.45	458.42
Cutting depth	2 mm	501.8	511.03
	1.5 mm	487.6	496.1
	0.5 mm	458	456.25

4. Conclusion

In this study, a fully-coupled temperature-displacement formulation was introduced, and the temperature-displacement interactions and dynamic instabilities of the high-speed peripheral milling of A2024-T351 aluminum alloy were investigated with the aid of a developed non-linear FE model. The developed model accurately captures severe plastic deformation and spatially and temporally evolving localized thermal gradients. The results of simulations indicated that technological parameters and kinematic tool mode significantly affect the development of the structure and thermal state of the cutting area. Generally, the highest cutting temperature grew with increasing the tooth number on the basis of the thermal steady-state obtained after four tooth engagements. In addition, a comparison study of the two cutter configurations demonstrated that climb milling had a lower thermal signature and a greater regularity of the force signal than conventional milling, indicating its potential benefits in thermal and process stability enhancement.

Most importantly, the time-dependent force history was directly coupled with frequency-domain Fast Fourier Transform (FFT) analysis that allowed the profound interpretation of the structural excitations. The spectral response was also seen to clearly separate the kinematically-forced tooth-passing frequency from the intrinsic high-frequency auto-excited phenomena associated with localized adiabatic shear banding and chip segmentation. The predictive power and physical fidelity of this computational framework had been substantiated via a blind comparison to experimental results over a range of cutting velocities, feed rates, and depths of cut, producing errors that did not exceed the 5% limit. Therefore, this model provided a strong basis for predicting stability lobes in HSM, reducing regenerative chatter, and increasing tool life.

Future investigations will extend this approach through experimental accelerometer and microphone measurements to formally correlate simulated force harmonics with physical sources of acoustic emission fields. In particular, the influence of tool geometry parameters, such as the number of cutting teeth, should be evaluated to investigate their effect on tooth-passing frequency, cutting-force fluctuations, and the interaction between kinematic excitation and chip segmentation dynamics. Further developments could also consider tool wear evolution, frictional conditions, and cooling strategies to improve the predictive capability of the proposed numerical framework.

Author contributions: Conceptualization, RS and LL; methodology, RS and LL; software, RS; validation, RS; formal analysis, RS; investigation, RS and LL; resources, RS, AR and AA; data curation, RS; writing—original draft preparation, RS; writing—review and editing, R.S. and LL; visualization, RS; supervision, LL; project administration: SB. This is a research result of this group. All authors have read and approved the final version of the manuscript.

Funding: This work received no external funding.

Institutional review board statement: Not applicable.

Informed consent statement: Not applicable.

Data availability statement: The data used in this study are available from the corresponding author upon reasonable request.

Conflict of interest: The authors declare no conflict of interest.

AI use statement: During the preparation of this manuscript, the authors used Google Gemini solely for language refinement. No AI tools were used for data analysis, interpretation, or generation of scientific content. All outputs were critically reviewed and edited by the authors. The authors take full responsibility for the integrity and accuracy of the work.

References

1. Wu D, Bai H, Zhao C, et al. High-speed micro-machining of T2 copper: Modelling and validation. International Journal of Simulation Modelling. 2026; 25(1): 123–133.
2. Ezugwu E. High Speed Machining of Aero-Engine Alloys. Journal of the Brazilian Society of Mechanical Sciences and Engineering. 2004; 26(1).
3. Xu J, An QL, Chen M. Analysis on Milling Performance of 2024-T351 Aluminum Alloy Using TiAlN Coated Carbide Cutting Tools. Materials Science Forum. 2011; 697–698: 218–222.
4. Calamaz M, Coupard D, Girot, F. A new material model for 2D numerical simulation of serrated chip formation when machining titanium alloy Ti–6Al–4V. International Journal of Machine Tools and Manufacture. 2008; 48:

275–288.
5. Klamecki B. Incipient Chip Formation in Metal Cutting—A Three-Dimension Finite Element Analysis [PhD thesis]. University of Illinois at Urbana-Champaign; 1973.
6. Komvopoulos K, Erpenbeck SA. Finite element modeling of orthogonal metal cutting. Journal of Engineering for Industry. 1991; 113(3): 253–267.
7. Piska M, Zouhar J. Modeling the orthogonal machining process using cutting tools with different geometry. Modern Machinery Science Journal. 2008; 48–52.
8. Grzesik W, Zalisz Z, Nieslony P. Friction and wear testing of multilayer coatings on carbide substrates for dry machining applications. Surface and Coatings Technology. 2002; 15: 37–45.
9. Perrelli M, Cosco F, Gagliardi F, et al. In-Process Chatter Detection Using Signal Analysis in Frequency and Time-Frequency Domain. Machines. 2022; 10(1): 24.
10. Navarro-Devia JH, Chen Y, Dao DV, et al. Chatter detection in milling processes—A review on signal processing and condition classification. The International Journal of Advanced Manufacturing Technology. 2023; 125: 3943–3980.
11. Rodríguez JM, Carbonell JM, Jonsén P. Numerical Methods for the Modelling of Chip Formation. Archives of Computational Methods in Engineering. 2020; 27(2): 387–412.
12. Nguyen HP, Derewońko A, Niezgoda T. Thermal Mechanical Coupled Simulation. Journal of KONES Powertrain and Transport. 2015; 22(3): 161–168.
13. Meng X, Lin Y, Mi S. An Improved Johnson–Cook Constitutive Model and Its Experiment Validation on Cutting Force of ADC12 Aluminum Alloy During High Speed Milling. Metals. 2020; 10(8): 1038.
14. Yeh YP, Tsai HH, Chang JY. Machine-Learning-Based Optimal Feed Rate Determination in Machining: Integrating GA-Calibrated Cutting Force Modeling and Vibration Analysis. Applied Sciences. 2025; 15(11): 6359.
15. Gao P, Zhu Y, Zhang H, et al. Cortical Bone Longitudinal-Torsional Ultrasonic Vibration-Assisted Milling for Multi-Tooth Cutter under Flexible Fixation Condition. Chinese Journal of Mechanical Engineering. 2026; 100237.
16. Deng WJ, Xie ZC, Li Q, et al. Finite element modelling and simulation of chip breaking with grooved tool. International Journal of Simulation Modelling. 2013; 12(4): 264–275.
17. Paresi PR, Narayanan A, Lou Y, et al. Finite Element Modeling for Orthogonal Machining of AA2024-T351 Alloy with an Advanced Fracture Criterion. Journal of Manufacturing Science and Engineering. 2021; 143(11): 111003.
18. Gunsalam H, Abdullah AS, Awi M, et al. Comparison between Johnson Cook's Plasticity with Damage Model and Isotropic Hardening Plasticity with Ductile Damage Model on Aluminium Alloy Sheet 2024 T3 Tensile Test in Correlating the Finite Element Method (FEM) to the Experiment Test Result. Jurnal Mekanikal. 2023; 46(2): 102–113.
19. Tamizharasan T, Senthil Kumar N. Optimization of Cutting Insert Geometry Using DEFORM 3D: Numerical Simulation and Experimental Validation. International Journal of Simulation Modelling. 2012; 11(2): 65–76.
20. Rathore MF, Ahmed A, Saleem W. FE parametric evaluation of macro to microscale dry milling for sustainable manufacturing of aerospace alloys. Results in Materials. 2024; 21: 100531.
21. Priyadarshini A, Pal SK, Samantaray AK. Finite Element Modeling of Chip Formation in Orthogonal Machining. In: Davim JP (editor). Statistical and Computational Techniques in Manufacturing. Springer; 2012. pp. 101–144.
22. Bermudo Gamboa C, Andersson T, Svensson D, et al. Modeling of the fracture energy on the finite element simulation in Ti6Al4V alloy machining. Scientific Reports. 2021; 11: 18490.
23. List G, Sutter G, Bouthiche A. Cutting temperature prediction in high speed machining by numerical modelling of chip formation and its dependence with crater wear. International Journal of Machine Tools and Manufacture. 2012; 54–55: 1–9.
24. Arrazola PJ, Özel T, Umbrello D, et al. Recent advances in modelling of metal machining processes. CIRP Annals–Manufacturing Technology. 2013; 62(2): 695–718.
25. Chen T, Li C, Zou Z, et al. An Advanced Approach for Predicting Workpiece Surface Roughness Using Finite Element Method and Image Processing Techniques. Machines. 2024; 12(11): 827.